



HAL
open science

Hydraulic tomography in coupled discrete-continuum concept to image hydraulic properties of a fractured and karstified aquifer (Lez aquifer, France)

P. Fischer, Abderrahim Jardani, H. Jourde

► **To cite this version:**

P. Fischer, Abderrahim Jardani, H. Jourde. Hydraulic tomography in coupled discrete-continuum concept to image hydraulic properties of a fractured and karstified aquifer (Lez aquifer, France). *Advances in Water Resources*, 2020, 137, pp.103523. 10.1016/j.advwatres.2020.103523. hal-02548914

HAL Id: hal-02548914

<https://normandie-univ.hal.science/hal-02548914v1>

Submitted on 21 Jul 2022

HAL is a multi-disciplinary open access archive for the deposit and dissemination of scientific research documents, whether they are published or not. The documents may come from teaching and research institutions in France or abroad, or from public or private research centers.

L'archive ouverte pluridisciplinaire **HAL**, est destinée au dépôt et à la diffusion de documents scientifiques de niveau recherche, publiés ou non, émanant des établissements d'enseignement et de recherche français ou étrangers, des laboratoires publics ou privés.



Distributed under a Creative Commons Attribution - NonCommercial 4.0 International License

Research Paper/

Hydraulic Tomography in Coupled Discrete-Continuum Concept to Image Hydraulic Properties of a Fractured and Karstified Aquifer (Lez Aquifer, France)

P. Fischer¹, A. Jardani¹, H. Jourde²

(1) Normandie Univ, UNIROUEN, UNICAEN, CNRS, M2C, 76000 Rouen, France

(2) Université de Montpellier, CNRS, Laboratoire Hydrosociences, 34000 Montpellier, France

Conflict of interest: None

Corresponding author: P. Fischer

E-mail : pierre.fischer1@univ-rouen.fr

Key words: Inverse problem, Karst, Fractures, Discrete network, Pumping test, Hydraulic tomography

Intended for publication in Advances in Water Resources

1 **Abstract**

2 We present the results of a hydraulic tomography led on a 60×40 m² fractured and karstic field
3 in Southern France in order to image, in a model, its transmissivity field. The dataset employed
4 for the tomography consists in drawdown responses to cross-boreholes pumping tests reaching
5 pseudo steady-state, with 8 different pumping wells and 22 measurement boreholes. The
6 inversion of the dataset was led on a 2D model coupling a discrete network and a continuum,
7 by following the Discrete Network Deterministic Inversion (DNDI) method. This method
8 permits an optimization of both the transmissivity distribution and the structural geometry of
9 the discrete network, which represents in this case the interconnected fractures and conduits in
10 the aquifer. The optimized model obtained after inversion allows reproducing the observed
11 drawdown in the field, and proposes a contrasted imaging of the hydraulic properties, as awaited
12 in such fractured site. The fracture network in the optimized model also shows coherent
13 orientations of fracturing, compared to the orientations effectively observed on the field, even
14 though this information was not included in the inversion. A comparison of the results obtained
15 with this coupled model to results obtained on the same data with equivalent porous media
16 model (without integration of a discrete network) shows that the integration of a discrete
17 network in the model greatly improves the ability of the model to reproduce the flows existing
18 in such fractured fields, and thus the observed drawdowns.

19 **1. Introduction**

20 Characterization of the subsurface field hydraulic properties represents an important
21 problematic for the hydrogeologists and engineers. In fact, the spatial distribution of the values
22 of hydraulic properties, such as transmissivity, strongly influences the subsurface flows. The
23 assessment of these underground properties usually requires to analyze responses to a
24 solicitation of the field, such as drawdown responses to a groundwater pumping (Batu 1998),
25 or other solicitations such as injections, slug tests, tracers as described in Butler (2005).

26 Therefore, the spatialization of the transmissivity values can be caught, among other methods,
27 by simultaneously analyzing the responses to pumping tests led in different boreholes from the
28 same field. This is typically realized by a hydraulic tomography approach (Yeh and Lee 2007).
29 In this approach, a large set of responses to cross-borehole pumping tests is associated with an
30 inversion process, in order to map a transmissivity field in a model which is then able to
31 reproduce the observed drawdowns when solving the flow equation (Illman et al. 2009; Cardiff
32 and Barrash 2011; Cardiff et al. 2013; Fischer et al. 2017a).

33 Hydraulic tomography appears as a powerful tool for the characterization of fractured fields
34 hydraulic properties. In fact, in fractured aquifers, the groundwater flow paths are mostly
35 constrained in the network of fractures, because these fractures generate a local increase in the
36 conductivity field. This leads to high contrasts in hydraulic properties, with a high conductivity
37 fracture network surrounded by a lower conductivity rock matrix. Illman (2014) reviewed and
38 highlighted the advantages brought by hydraulic tomography for the assessment of these
39 contrasts in fractured site. The scientific literature contains several works of hydraulic
40 tomography on fractured fields, some of these works being listed hereafter. One main difference
41 between these works concerns the representation of the heterogeneity within the transmissivity
42 field in the model.

43 One of the approaches is to represent this heterogeneity with a single continuum in which the
44 fractures and matrix properties are approximated with an equivalent hydraulic conductivity
45 field. In this case, the solution of the inversion should be constrained in order to produce the
46 expected contrast in the transmissivity field. Thus, Hao et al. (2008) and Sharmeen et al. (2012)
47 have used the Sequential Successive Linear Estimator developed by Yeh and Liu (2000) to
48 image the conductivity fields of, respectively, a synthetic fractured case and a fractured rock
49 block in laboratory. The same approach was also tested more recently by Mohammadi and
50 Illman (2019) on a synthetic karstic conduit network. Other possible inversion constraints for
51 single continuum modeling have been tested on a same dataset from a fractured and karstified
52 field in France: the transitional-probability generation (Wang et al. 2017), the sparse non-linear
53 optimizer (Wang et al. 2016) and a cellular automata-based approach (Fischer et al. 2017b).
54 Single continuum 3D hydraulic tomography applications have been proposed by Illman et al.
55 (2009) and Zha et al. (2015) for a large fractured field in Japan, and more recently for a fractured
56 rock unit at a smaller scale by Tiedeman and Barrash (2019). A dual continuum, considering
57 two linked continuum (one for the matrix and one for the fractures), has been proposed in
58 Trottier et al. (2014) as an alternative to the single continuum representation.

59 Another possible representation for the imagery of fractured fields requires the integration of a
60 discrete network in the model. In this case, a network of lines or planes representing the
61 fractures is included in a 2D or 3D continuum which represents the matrix. The matrix can be
62 considered as impermeable, leading to water fluxes only in the fracture networks, or a low
63 permeability background in a coupled model, allowing for flows also in the matrix. This type
64 of representation has been adopted to infer the hydraulic properties of a simplified fracture
65 network, positioned in the model based on connectivity information, in Klepikova et al. (2013)
66 and Klepikova et al. (2014). However, the main difficulty arising from this representation
67 remains the construction of the discrete network within the model. In fact, in this case, not only

68 the property values of the fractures are important, but also their positioning and their
69 connectivity. Therefore, when the information related to the fractures positioning is limited, it
70 may be necessary to optimize the network geometry in the model as well. This can be achieved
71 by generating networks stochastically from field information such as statistical (Cacas et al.
72 1990), mechanical (Josnin et al. 2002; Bonneau et al. 2013) or speleological templates (Pardo-
73 Iguzquiza et al. 2012) information. More recently, Somogyvari et al. (2017) have proposed to
74 optimize the discrete network with a method based on a reversible jump Markov Chain Monte
75 Carlo, which allows for iterative semi-random updates of its geometry, based on statistical
76 information. However, a deterministic optimization of the network of fractures is less common
77 in the literature. Such a method to optimize the geometry of a network of interconnected
78 fractures in a deterministic way has been proposed in Fischer et al. (2018a) and tested on
79 synthetic cases.

80 Several works have discussed the importance of integrating discrete networks for the modeling
81 of flows in fractured or karstic aquifers, compared to single continuum models. Among them,
82 Kovacs (2003) noticed that, for a karstic aquifer at a watershed scale (kilometric), only the
83 presence of discrete networks in the model could permit to reproduce in a same time the
84 observed heads and the observed spring discharges. More recently, Dong et al. (2019) studied
85 the conditions to obtain an equivalence between inverted single continuum simulations and
86 simulations obtained from a synthetic discrete fracture network model. They have observed
87 that, if the scale of the investigation within a fractured medium reaches the Representative
88 Elementary Volume (REV), then a single continuum model could provide good inversion
89 results. However, if the scale was below the REV and the observation wells were limited, a
90 single continuum model permitted to only identify the dominant fractures.

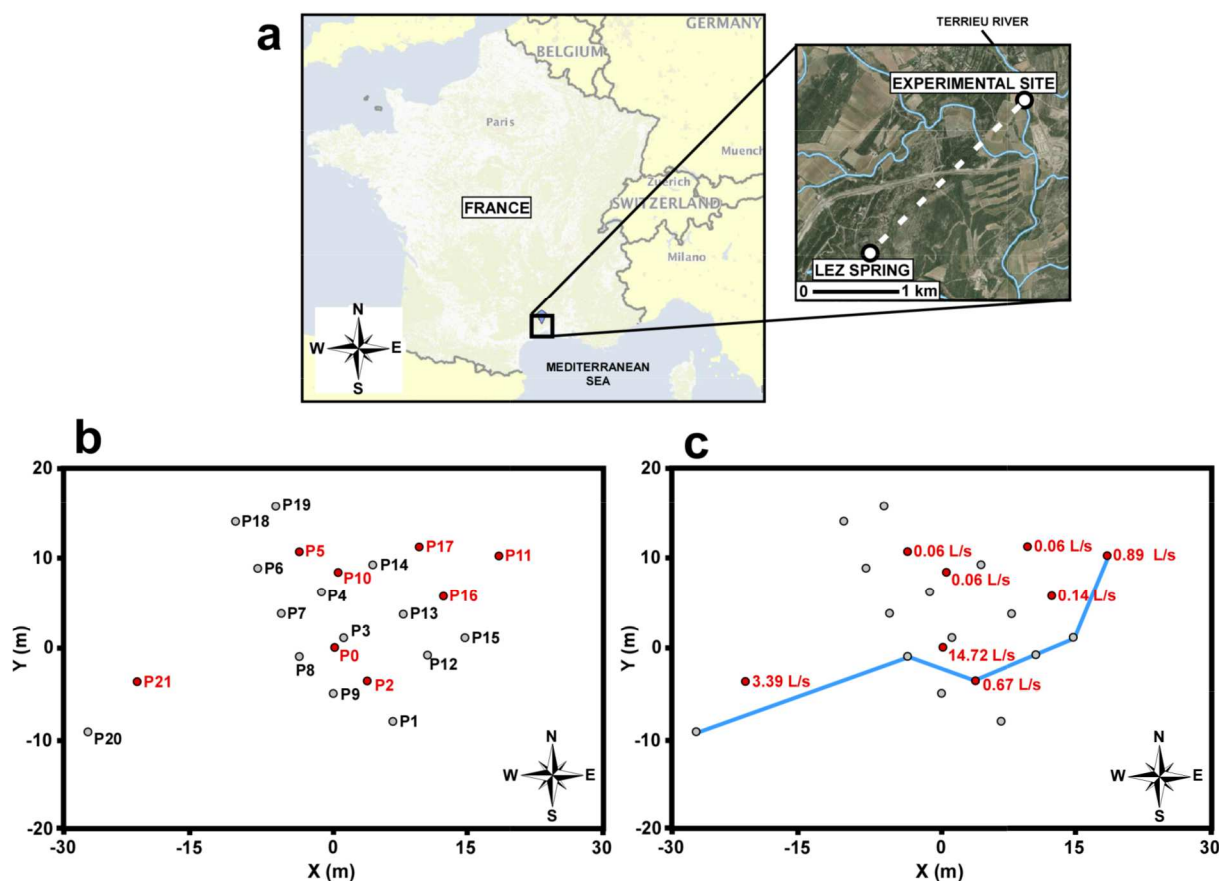
91 In this work, we aim to contribute to this discussion comparing single continuum and discrete
92 network modeling approaches for the representation of a fractured field in a hydraulic

93 tomography. For this purpose, we will apply the Discrete Network Deterministic Inversion
94 (DNDI) method proposed in Fischer et al. (2018a) on steady-state drawdown responses
95 obtained, at a decametric scale, on the Terrieu fractured and karstified field, in France. The
96 results obtained from the discrete network modeling in this work will then be compared to those
97 obtained from a more classical single continuum modeling. These comparison will allow us to
98 discuss the benefits of including discrete networks in the model for the representation of
99 fractures/conduits networks at a decametric scale. In this paper, we will first briefly present the
100 Terrieu site, and the drawdown dataset used for its characterization. Then, we will expose the
101 parameterization of the transmissivity field in the model for the DNDI method and its associated
102 deterministic inversion for the optimization of both the network geometry and the transmissivity
103 values. In the last section we will present the results obtained with the DNDI approach, and
104 discuss its differences, benefits and limits to those obtained from other approaches without
105 discrete networks.

106

107 **2. Site presentation**

108 The Terrieu experimental field is located on the MEDYCYSS observation site (Jourde et al.
109 2011), part of the Karst observatory network (Jourde et al. 2018) initiated by the French institute
110 INSU/CNRS. This well-known site has been recently studied in two PhD-thesis (Jazayeri
111 Noushabadi 2009 and Dausse 2015) and characterized through different tomographic
112 approaches (Wang et al. 2016; Wang et al. 2017; Fischer et al. 2017b; Fischer et al. 2018b).
113 This field is located in Southern France, at the North of the city Montpellier (see Figure 1). It
114 is part of the karstic and fractured Lez regional aquifer, whose spring is located a few kilometers
115 downstream.



116

117 Figure 1: (a) Localization of the Terrieu experimental site in France, near the town of
 118 Montpellier. This karstic site is part of the regional Lez aquifer and hydraulically connected to
 119 the Lez spring. Maps of (b) the boreholes on the Terrieu experimental site and (c) the pumping
 120 rates applied in 8 boreholes during the investigation. Boreholes represented by red dots are
 121 pumping/measurement wells, and boreholes represented by grey dots are only measurement
 122 wells. The boreholes linked with a blue line are known to be well connected within the karst
 123 network, according to Dausse (2015).

124

125 The Terrieu field extends over an area of approximately 2,500 m² and is equipped with 22
 126 boreholes distributed over this area, as presented in Figure 1b. Geological logs in these
 127 boreholes indicate that the field is composed of thin-layered marly limestones on its upper part
 128 and massive limestones below. The interface between these two units is a slope monocline
 129 fractured plane dipping at 20° Nord-West, and present at depths between 35 and 45 m above
 130 the field surface. The fractures have an ENE-WSW global direction and a less important SE-
 131 NW secondary direction (Wang et al. 2016).

132 Characterization investigations (temperature logs, electrical conductivity logs, and packer tests)
133 presented in Jazayeri Noushabadi (2009), Jazayeri Noushabadi (2011) and Dausse (2015) have
134 highlighted the fact that the groundwater flows in this field were mostly constrained to the
135 interface between the two geological units (Dausse et al. (accepted 2019)). Wells downhole
136 videos have indeed shown that a karstic network had preferentially developed within this sloped
137 bedding plane, with conduits' aperture up to 25 cm width. Because of the low permeability of
138 the rocks units on both sides of this fractured interface, the aquifer part on this field is supposed
139 to be confined. The previous investigations also permitted to show that several boreholes of the
140 site were well connected through this karstic network. This known connectivity is presented in
141 Figure 1c with a blue line, linking the connected boreholes.

142 The dataset employed for the hydraulic tomography approach presented in this article has been
143 obtained from a cross-boreholes pumping investigation performed within the framework of
144 Jazayeri Noushabadi's PhD. Eight alternated constant-rate pumping tests have been performed
145 on the field, in the boreholes and with the pumping rates indicated in red in Figure 1c. The
146 groundwater level during the different pumping tests was always kept above 35 m below the
147 surface, which means that the fractured and karstified horizon was continuously saturated.
148 During the pumping phases, the drawdowns were measured continuously in all wells in the
149 fields with CTD-diver probes. The pseudo steady-state (approaching the steady state)
150 drawdown responses measured in each well and for each pumping (a total of 176 data)
151 constitute the dataset used for the modeling of flow field, presented in the next section.

152

153 **3. Algorithm presentation**

154 **3.1. Forward problem and model parameterization**

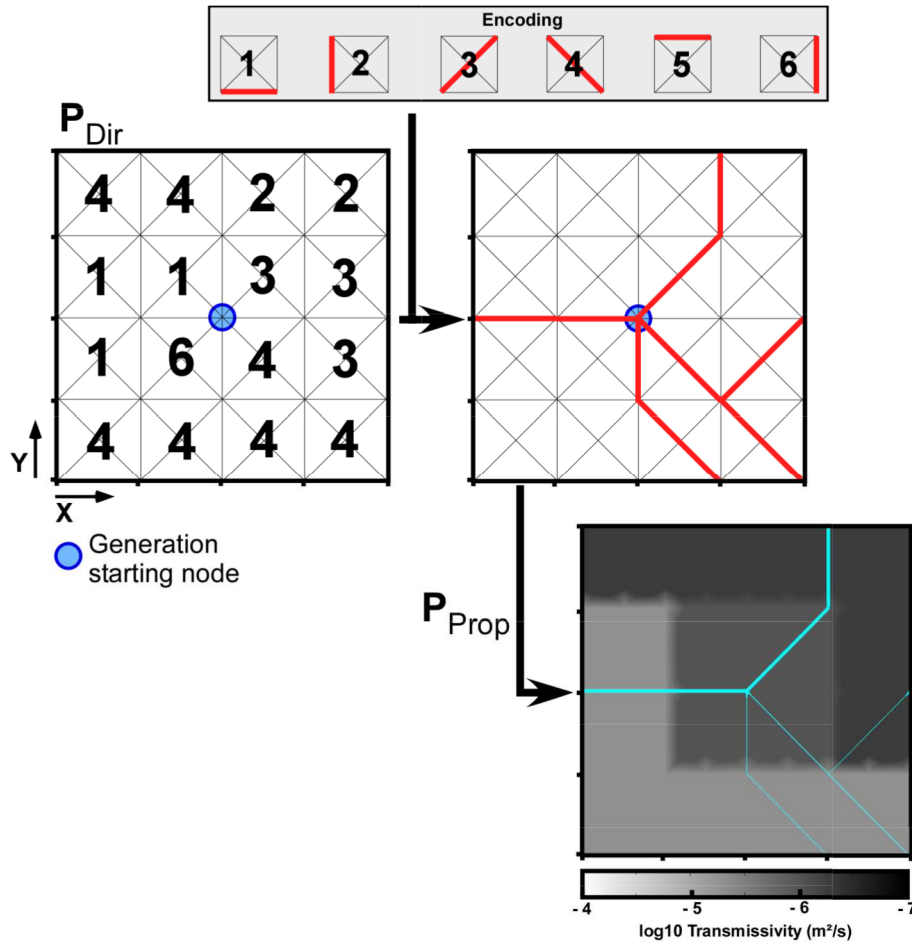
155 The hydraulic tomography approach presented in this article has been performed with the
 156 Discrete Network Deterministic Inversion (DNNDI) algorithm, as presented in Fischer et al.
 157 (2018a). The DNNDI method is based on a coupled discrete-continuum model Γ in which the
 158 transmissivity is distributed over of a 1D discrete network Γ_N representing the
 159 karstic/fractures flows and a 2D continuum Γ_M representing the flows in the matrix rock. The
 160 forward problem f consists in solving the flows continuity equations in a steady state by
 161 considering the Darcy's formulation in both parts:

$$162 \quad \left\{ \begin{array}{l} \nabla \cdot (-T_M \cdot \nabla h) = \frac{Q_M}{S_{el.}} \quad \text{in the matrix } \Gamma_M \\ \nabla_T \cdot (-T_N \cdot \nabla_T h) = \frac{Q_N}{S_{el.}} \quad \text{in the network } \Gamma_N \end{array} \right. , \quad (1)$$

163 with T_M, T_N the equivalent transmissivities of the matrix rock and of the fractures (m^2/s), h the
 164 piezometric level (m), Q_M, Q_N punctual extractions rates (m^3/s) at pumping locations, and $S_{el.}$
 165 a model elementary surface at the given pumping locations (m^2). ∇_T is the tangential gradient
 166 along the discrete elements of the model.

167 The coupled model is partitioned in p_X squared subspaces along the X-axis, and p_Y along
 168 the Y-axis (for a total of $p = p_X \times p_Y$ subspaces). The position of the discrete network in the
 169 model and the distribution of the transmissivities among the background and the fractures are
 170 piloted by two vectors of parameters: \mathbf{P}_{Dir} and \mathbf{P}_{Prop} (Figure 2). \mathbf{P}_{Dir} is a p -vector (i.e. of
 171 dimension $p \times 1$) containing the local directions of the network for each subspace of the model,
 172 following an established encoding (see Encoding in Figure 2). The generation of the network
 173 follows a 'node-to-node' principle. The encoding defines, for each subspace, how the network

174 should propagate in it (one over six possible directions) if one of its node (a corner between
 175 subspaces) becomes activated during the generation process. The generation starts at a chosen
 176 node which is initially considered as 'activated'. If a subspace connected to this 'activated'
 177 node is encoded with a local direction going through this node, the network propagates in the
 178 direction assigned to this area of the model. The node newly reached by the generated network
 179 becomes 'activated', allowing the generation of the network in new subspaces, while the
 180 subspace in which the generation has already occurred becomes inhibited to another generation.
 181 The 'node-to-node' generation process continues until there is no more newly 'activated' nodes.
 182 Some of the subspaces may not participate in the generation of the network in the end, if none
 183 of their nodes is activated during the process, or if their nodes activated during the generation
 184 are not involved in their encoded direction (leading to a 'no fracture' possibility). \mathbf{P}_{Prop} is a $2p$
 185 -vector containing the local values of transmissivity for the background (matrix) and fracture
 186 parts in each subspace. Thus, a model Γ can be generated and locally modified in an easy way
 187 through the values contained in \mathbf{P}_{Dir} and \mathbf{P}_{Prop} . A model defined with these two parameters is
 188 noted $\Gamma(\mathbf{P}_{\text{Dir}}, \mathbf{P}_{\text{Prop}})$.



189

190 Figure 2: Schematic representation of the model parameterization in the DNDI method. The
 191 geometry of the discrete network is encoded in a \mathbf{P}_{Dir} vector and the transmissivity values
 192 associated to each part of the matrix and discrete network in the model are encoded in a \mathbf{P}_{Prop}
 193 vector.

194

195 Solving the forward problem presented in Eq. 1 for a parameterized coupled model, as presented
 196 in Figure 2, permits to simulate the map of piezometric levels. In this work, we simulate the
 197 piezometric levels with the software COMSOL Multiphysics, considering an adaptive
 198 triangular mesh (sizes between $0.06 m^2$ and $1.5 m^2$) for the finite-element resolution of Eq.1. In
 199 our case, the piezometric levels will allow to assess the drawdowns, generated from the
 200 pumping tests, at the given measurement points:

201

$$\mathbf{d} = f \left(\Gamma \left(\mathbf{P}_{Dir}, \mathbf{P}_{Prop} \right) \right) + \boldsymbol{\varepsilon}, \quad (2)$$

202 where \mathbf{d} is a n -vector of simulated drawdowns at different locations, f is the forward
 203 problem described in Eq. 1, $\Gamma(\mathbf{P}_{\text{Dir}}, \mathbf{P}_{\text{Prop}})$ is a parameterized coupled model and $\boldsymbol{\epsilon}$ is a
 204 Gaussian noise with a zero mean for adding noise to the data and prevent an overfitting of the
 205 inversion.

206 3.2. Inverse problem

207 The inverse problem involves the use of a forward problem in the optimization process in order
 208 to find a possible solution of the parameters \mathbf{P}_{Dir} and \mathbf{P}_{Prop} . In a Bayesian framework, this
 209 consists in defining a model able to reproduce the set of observed drawdowns, while also
 210 respecting some prior properties information.

211 Our deterministic inversion process is sequential and iterative. After each step, the parameters
 212 are modified in order to reduce the values of the objective functions (Tarantola and Valette
 213 1982):

$$214 \quad \Psi_{\text{network}}(\mathbf{P}_{\text{Dir}}) = \frac{1}{2} \left(\mathbf{d}_{\text{obs}} - f(\Gamma(\mathbf{P}_{\text{Dir}}, \mathbf{P}_{\text{Prop}})) \right)^T \mathbf{C}_d^{-1} \left(\mathbf{d}_{\text{obs}} - f(\Gamma(\mathbf{P}_{\text{Dir}}, \mathbf{P}_{\text{Prop}})) \right) \quad (3)$$

$$+ \frac{1}{2} \left(\mathbf{P}_{\text{Dir}, \text{prior}} - \mathbf{P}_{\text{Dir}} \right)^T \mathbf{C}_{\mathbf{P}_{\text{Dir}}}^{-1} \left(\mathbf{P}_{\text{Dir}, \text{prior}} - \mathbf{P}_{\text{Dir}} \right)$$

$$215 \quad \Psi_{\text{properties}}(\mathbf{P}_{\text{Prop}}) = \frac{1}{2} \left(\mathbf{d}_{\text{obs}} - f(\Gamma(\mathbf{P}_{\text{Dir}}, \mathbf{P}_{\text{Prop}})) \right)^T \mathbf{C}_d^{-1} \left(\mathbf{d}_{\text{obs}} - f(\Gamma(\mathbf{P}_{\text{Dir}}, \mathbf{P}_{\text{Prop}})) \right) \quad (4)$$

$$+ \frac{1}{2} \left(\mathbf{P}_{\text{Prop}, \text{prior}} - \mathbf{P}_{\text{Prop}} \right)^T \mathbf{C}_{\mathbf{P}_{\text{Prop}}}^{-1} \left(\mathbf{P}_{\text{Prop}, \text{prior}} - \mathbf{P}_{\text{Prop}} \right)$$

216 with Ψ_{network} the structural objective function, $\Psi_{\text{properties}}$ the properties objective function, \mathbf{d}_{obs}
 217 a n -vector of observed drawdown to be reproduced by the model, $\mathbf{P}_{\text{Dir}, \text{prior}}$ and $\mathbf{P}_{\text{Prop}, \text{prior}}$ are
 218 vectors of a priori parameter values to constrain the optimization, \mathbf{C}_d is a $n \times n$ covariance

219 matrix on the drawdown data, and $\mathbf{C}_{\mathbf{P}_{\text{Dir}}}$ and $\mathbf{C}_{\mathbf{P}_{\text{Prop}}}$ are $p \times p$ and $2p \times 2p$ covariance matrices
 220 on the parameters values.

221 The deterministic inversion process is initialized with chosen values for the structural parameter
 222 \mathbf{P}_{Dir} and the property parameter \mathbf{P}_{Prop} . The initial property values should be chosen wisely as,
 223 in a deterministic process, the initial model determines the local solution to which the process
 224 will converge. Then, the optimization part permits to modify the parameters \mathbf{P}_{Dir} and \mathbf{P}_{Prop} in
 225 order to minimize the objective functions. The parameters are not optimized simultaneously,
 226 we use a sequential inversion, modifying first \mathbf{P}_{Dir} by considering the initial \mathbf{P}_{Prop} and the
 227 objective function in Eq. 3, and then modifying \mathbf{P}_{Prop} by considering the previously inverted
 228 \mathbf{P}_{Dir} and the objective function in Eq. 4. Finally the inversion process finishes with a posterior
 229 sensitivity analysis on the resulting model.

230 3.3. Optimization and uncertainties estimation

231 The parameters contained in \mathbf{P}_{Dir} and \mathbf{P}_{Prop} are modified iteratively in the sequential
 232 optimization part of the inverse process. This part modifies the parameters in order to minimize
 233 the objective functions in Eq. 3 and Eq. 4 by using sensitivity analyses.

234 Firstly, the structural parameter \mathbf{P}_{Dir} is optimized, while we consider the initial \mathbf{P}_{Prop} as constant.

235 For a given iteration k , the optimization of $\mathbf{P}_{\text{Dir}}^k$ uses a sensitivity analysis contained in a $6 \times p$

236 matrix \mathbf{J}_n^k generated, for an element (i, j) of the matrix, as follow:

$$237 \mathbf{J}_n^k(i, j) = \frac{1}{2} \left(\mathbf{d}_{\text{obs}} - f \left(\Gamma \left(\mathbf{P}_{\text{Dir}}^k \Big|_{\mathbf{P}_{\text{Dir}}(j)=i}, \mathbf{P}_{\text{Prop}} \right) \right) \right)^T \mathbf{C}_d^{-1} \left(\mathbf{d}_{\text{obs}} - f \left(\Gamma \left(\mathbf{P}_{\text{Dir}}^k \Big|_{\mathbf{P}_{\text{Dir}}(j)=i}, \mathbf{P}_{\text{Prop}} \right) \right) \right) + \frac{1}{2} \left(\mathbf{P}_{\text{Dir}, \text{prior}}(j) - i \right)^T \mathbf{C}_{\mathbf{P}_{\text{Dir}}}^{-1} \left(\mathbf{P}_{\text{Dir}, \text{prior}}(j) - i \right) \quad (5)$$

238 with $\Gamma\left(\mathbf{P}_{\text{Dir}}^k \mid \mathbf{p}_{\text{Dir}(j)=i}, \mathbf{P}_{\text{Prop}}\right)$ the model generated through a modification of the local direction i
 239 (among the 6 possible as encoded in Figure 2) in the subspace j of the model (among the p
 240 subspaces of the model).

241 $\mathbf{p}_{\text{Dir}}^k$ is updated from the minimum value found in \mathbf{J}_n^k . The minimum value represents the best
 242 minimization of the objective function in Eq. 3 for this iteration, and its position $(\hat{i}_{\min}, \hat{j}_{\min})$ in
 243 the matrix represents the modification of local direction (\hat{i}_{\min}) in the subspace \hat{j}_{\min} that has to
 244 be produced to generate $\mathbf{p}_{\text{Dir}}^{k+1}$. The iterative process continues until no more minimization can
 245 be found through the structural parameter for the objective function in Eq. 3.

246 After the optimization part, the distribution of the structural posterior uncertainties can be
 247 calculated for each subspace of the model in a p -vector $\mathbf{C}_{\text{Dir}}^{\text{post}}$:

$$248 \quad \mathbf{C}_{\text{Dir}}^{\text{post}}(j) = \left(\frac{1}{6} \sum_{i=1}^6 \mathbf{J}_n^{\text{post}}(i, j) - \Psi_{\text{network}}^{\text{post}} + \mathbf{C}_{\text{Dir}}^{-1}(j, j) \right)^{-1}, \quad (6)$$

249 where $\mathbf{C}_{\text{Dir}}^{\text{post}}(j)$ denotes the structural posterior uncertainty value associated to the subspace j ,
 250 $\mathbf{J}_n^{\text{post}}$ is the structural sensitivity matrix of the last optimization iteration and $\Psi_{\text{network}}^{\text{post}}$ is the
 251 value of the structural objective function of the last optimization iteration.

252 Secondly, the property parameter \mathbf{P}_{Prop} is optimized, while we consider the previously optimized
 253 \mathbf{P}_{Dir} as constant. For a given iteration k , the optimization of $\mathbf{P}_{\text{Prop}}^k$ uses a linearization of the
 254 objective function in Eq. 4:

$$255 \quad \mathbf{P}_{\text{Prop}}^{k+1} = \mathbf{P}_{\text{Prop}}^k + \left(\left(\mathbf{J}_p^k \right)^T \cdot \mathbf{C}_d^{-1} \cdot \mathbf{J}_p^k + \mathbf{C}_{\text{Prop}}^{-1} \right)^{-1} \cdot \left(\left(\mathbf{J}_p^k \right)^T \cdot \mathbf{C}_d^{-1} \cdot \left(\mathbf{d}_{\text{obs}} - f\left(\Gamma\left(\mathbf{P}_{\text{Dir}}, \mathbf{P}_{\text{Prop}}^k\right)\right) \right) + \mathbf{C}_{\text{Prop}}^{-1} \cdot \left(\mathbf{P}_{\text{Prop}, \text{prior}} - \mathbf{P}_{\text{Prop}}^k \right) \right) \quad (7)$$

256 where \mathbf{J}_p^k is the $n \times 2p$ sensitivity matrix computed from a finite difference method:

$$257 \quad \mathbf{J}_p^k(i, j) = \left. \frac{\partial f_i}{\partial \mathbf{P}_{Prop}^k} \right|_{\mathbf{P}_{Prop}^k(j) = \mathbf{P}_{Prop}^k(j) + \Delta \mathbf{P}_{Prop}} \quad \text{where } \Delta \mathbf{P}_{Prop} \text{ is a finite difference step (in this application}$$

$$258 \quad \Delta \mathbf{P}_{Prop} = 10^{-4}).$$

259 The iterative process continues until the value of the objective function in Eq. 3 converges to a
260 minimum.

261 After the optimization part, a matrix of posterior covariance can be calculated as follow:

$$262 \quad \mathbf{C}_{P_{Prop}}^{post} = \left(\left(\mathbf{J}_p^{post} \right)^T \cdot \mathbf{C}_d^{-1} \cdot \mathbf{J}_p^{post} + \mathbf{C}_{P_{Prop}}^{-1} \right)^{-1}, \quad (8)$$

263 with \mathbf{J}_p^{post} is the sensitivity matrix of the last optimization iteration.

264 The standard deviation uncertainty associated to the property values of each subspace can be
265 inferred from the square root values of the diagonal entry of the posterior covariance matrix.

266

267 4. Application

268 4.1. Hydraulic tomography result

269 A 2D 60×40 m² model has represented a top-down view of the fractured interface plane from
270 the Terrieu experimental field. The model was surrounded by a large equivalent porous media
271 area ('buffer zone') in order to neglect the effect of the boundaries conditions on the drawdowns
272 in the model. The DNDI algorithm was coded in Matlab and linked to COMSOL Multiphysics
273 which solved the forward problem in steady state.

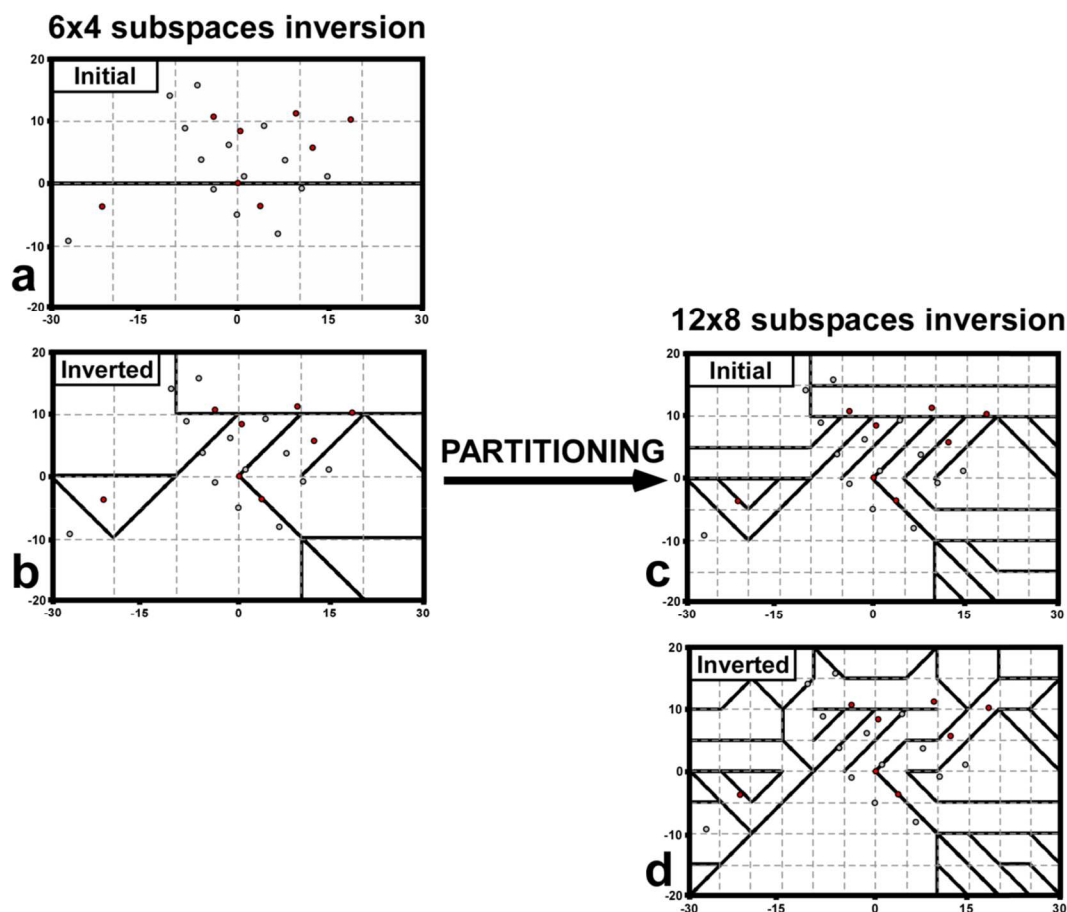
274 For the inversion, the parameters considered in \mathbf{p}_{Prop} were the transmissivity values in a \log_{10}
 275 scale ($\log_{10}(T)$). The values of transmissivities in the model were taken as initially uniform
 276 within the matrix (10^{-6} m²/s) and the fracture (10^{-1} m²/s). These initial values were also used as
 277 a priori values during the inversion in $\mathbf{p}_{\text{Prop,prior}}$. The transmissivity of the buffer zone was fixed
 278 for the whole inversion at a value 10^{-2} m²/s. These values were chosen accordingly to the
 279 previous studies and results obtained on this field (Wang et al. 2016 ; Fischer et al. 2017b). No
 280 a priori information concerning the fracture network local direction were considered in $\mathbf{p}_{\text{Dir,prior}}$
 281 .

282 The covariance matrices were constructed as diagonal matrices. Thus, we chose
 283 $\mathbf{C}_d = 10^{-2} \cdot \text{Id}(n)$, and $\mathbf{C}_{\text{Prop}} = \sigma \cdot \text{Id}(m)$ with $\sigma = 10^{-2}$ for the fracture \log_{10} -transmissivities
 284 and $\sigma = 1$ for the matrix \log_{10} -transmissivities.

285 The inversion was initialized with a model containing one single linear fracture, oriented East-
 286 West, with a starting node in coordinates 0;0 (see Figure 3). As the process is deterministic the
 287 initial model influences the inversion. In particular, starting from an initial model too ‘far’ from
 288 the solution might result in a non-convergence of the inversion.

289 A first partitioning of the model in 6×4 subspaces (i.e. 10×10 m² square subspaces) was
 290 chosen for the DNDI method. This partitioning was used for a first inversion (Figure 3a to 3b),
 291 whose result was then repartitioned and used as initial model for a second inversion (Figure 3c
 292 to 3d). This ‘multi-scale’ inversion has been already employed in previous works (Yoon et al.
 293 1999, Grimstadt et al. 2003) and permits to prioritize the flows in the model. In this way, the
 294 first inversion aimed to find the global trends of the discrete network, while the second inversion
 295 permitted to detail local parts of the network. In a deterministic problem this multi-scale
 296 approach accelerates the inversion process and facilitates its convergence to a local minimum

297 after partitioning. It is especially interesting for deterministic inversion problems of highly
 298 heterogeneous fields, which could easily diverge when the resolution of the model is too high
 299 (although this high amount of inversion parameters is necessary to represent the heterogeneity).



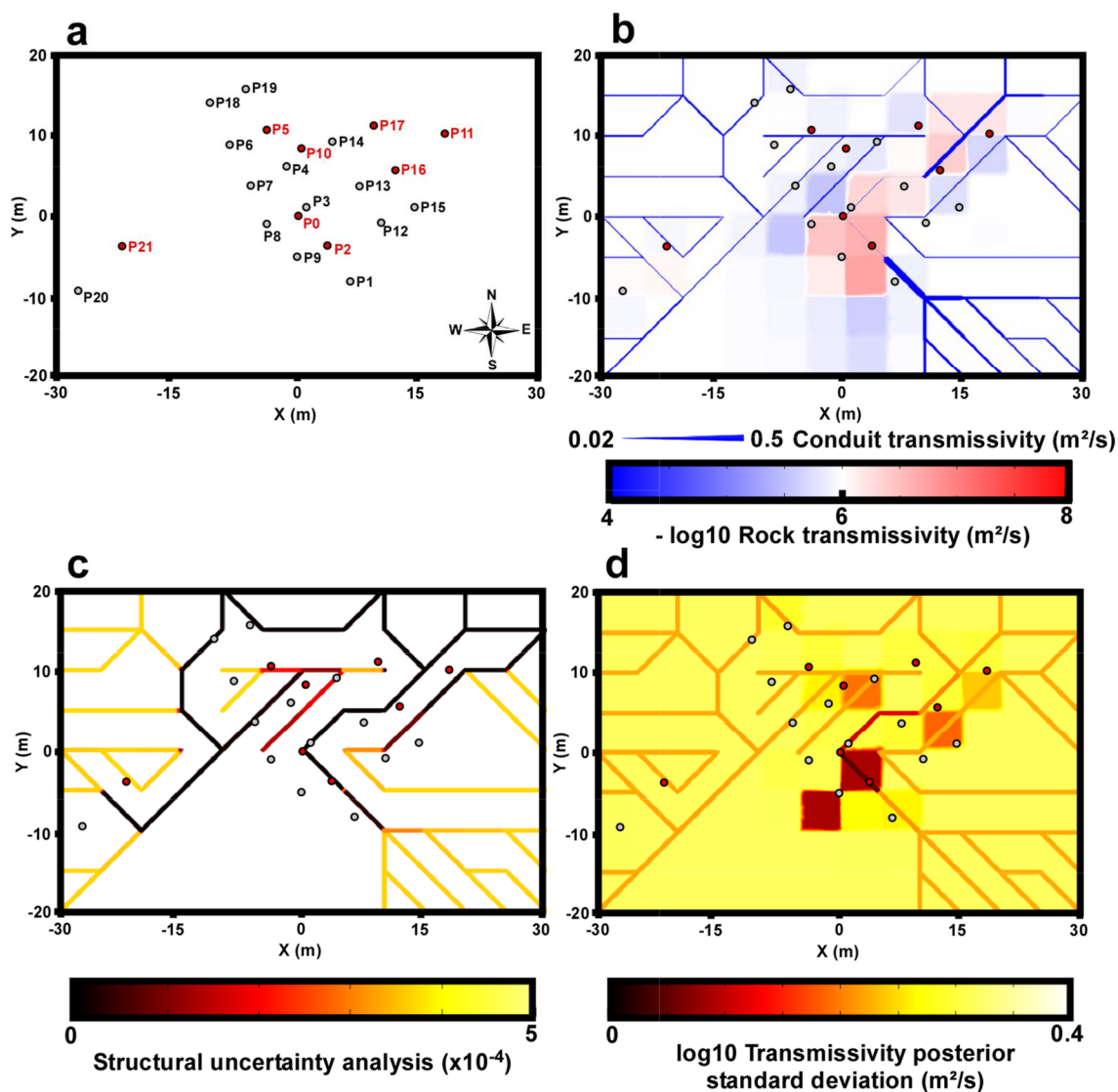
300

301 Figure 3: Schematic representation of the global inversion process, involving a first inversion
 302 starting with a 6×4 subspaces initial model (a), followed by a partitioning of the inversion
 303 resulting model into a 12×8 subspaces model (b to c). This partitioned model is then used as
 304 initial model for a second, more precise, inversion (c to d).

305

306 The solution to which the deterministic inversion converged, after optimization of the network
 307 geometry and the transmissivity values, is presented in Figure 4b. The result was obtained after
 308 32 structural iterations and 3 properties iterations. Figure 4c presents the maps of structural
 309 uncertainties associated to the solution. The lower the value of structural uncertainty, the better
 310 the local direction is constrained by the data (modifying this local direction would result in a

311 bad reproduction of the observed responses). Figure 4d presents the maps of transmissivity
 312 standard deviations associated to the solution.



313

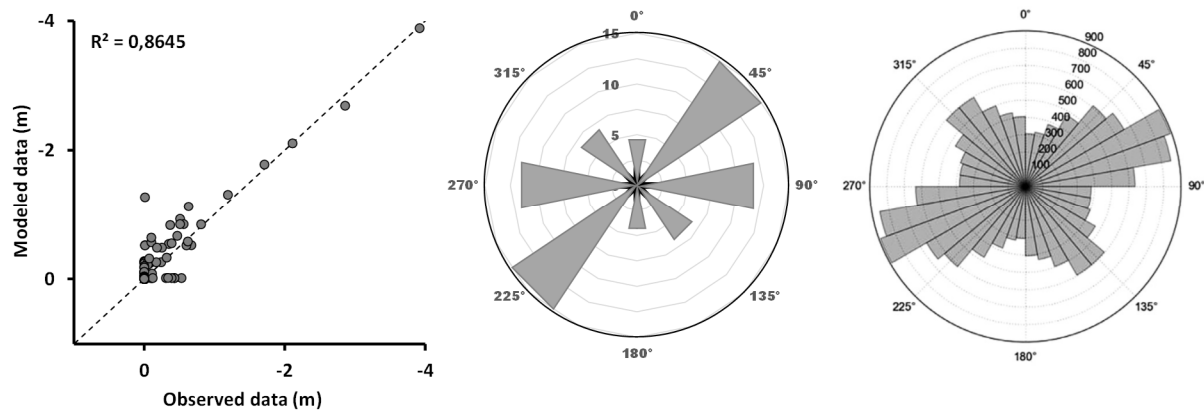
314 Figure 4: Maps of (a) the boreholes of the Terrieu site (in red the pumping wells), (b) the
 315 distribution of discrete network and transmissivity values obtained as result of the inversion,
 316 (c) the structural uncertainties on the discrete network obtained by inversion, and (d) the
 317 standard deviations on the transmissivity values obtained by inversion.

318

319 The distribution of transmissivities obtained after inversion presents a dense network of
 320 fractures in a heterogeneous matrix (Figure 4b). The network of fracture can appear as rather
 321 unrealistic, or simplistic, regarding the known morphology of fractures and karst conduits.

322 However, the DNDI method is purely based on flow data and no morphologic information was
323 provided to the inversion process. Therefore the network presented in the model shall mimic
324 only the interconnected fractures, influencing the groundwater flows induced by the pumping
325 in the field. The part of the fractures and conduits that do not contribute to these flows, like
326 dead end features for example, can logically not be retrieved with this inversion method.

327 The model permits a good reproduction of the drawdowns (Root Mean Square Error (RMSE)
328 of 0,18 m), except for the very small drawdowns (< 50 cm) (Figure 5). The uncertainties on the
329 geometry of the network (Figure 4c) indicate that the reproduction of the drawdowns is
330 conditioned to the local directions identified for a large part of the network in the central part
331 of the model. This indicated that, for the modeling of flows in a fractured media, a good
332 integration of the directions of the fractures is essential. The part of the network around P5 and
333 P6 appears as less constrained structurally, but according to previous works (Dausse 2015) this
334 area would be associated more likely to less important fractures and, thus, their orientations
335 might have less impact on the flows. The western part and south-eastern parts of the network
336 are not structurally constrained by the data, which means that the fractures orientations in these
337 parts don't play an important role in the reproduction of the observed drawdowns. However,
338 the inversion process brought some modifications in these parts of the network (densification
339 of the fractures network), which can be attributed to the simulation of more water income from
340 these parts of the model, indicating the existence of fractures which cannot be clearly identified
341 due to the absence of boreholes in these area. The uncertainty on the transmissivity values
342 (standard deviations in Figure 4d) have not been significantly lowered during the inversion
343 (except in some local parts in the center of the model). This is due to the fact that, in a fractured
344 and karstic field, the flows are more influenced by the orientation and localization of the
345 fractures/conduits, and the contrast of hydraulic properties between matrix and fractures rather
346 than by variations of property values within a fracture or in the matrix.



347

348 Figure 5: Scatterplot comparing the observed drawdowns to the drawdowns modeled with the
 349 distributed model obtained as result of the inversion, and graphs showing the orientations of the
 350 fractures in the model (left) and observed on the field (right; from Wang et al. 2016).

351

352 In Figure 5, we present graphs showing the orientations of fractures in the model and observed
 353 on field as described in Wang et al. (2016). For the orientation of the fractures in the model, we
 354 considered only the parts of the network which were structurally constrained by the model, as
 355 the orientations of the fractures in the other parts may not be representative. By comparing these
 356 two graphs it appears that the network obtained by inversion is rather coherent with the
 357 observed orientations of fracturing. The main orientations of fractures in the model are NE-SW
 358 and E-W, corresponding to the observed ENE-WSW orientations (which cannot be represented
 359 in the model through the DNDI method). Then, the NW-SE orientation is also represented in
 360 the model and represents a secondary direction of fracturing, while the N-S orientation concerns
 361 only a few part of the network, which is also coherent to the observations on the field. In the
 362 inversion process, these information of orientation could only be interpreted from the data, as
 363 the initial model integrated only one single fracture (oriented E-W) and no prior information
 364 concerning the fracture orientations were integrated in the inversion process. Therefore, this
 365 comparison between modeled and observed fracture network represents one form of validation
 366 of the model.

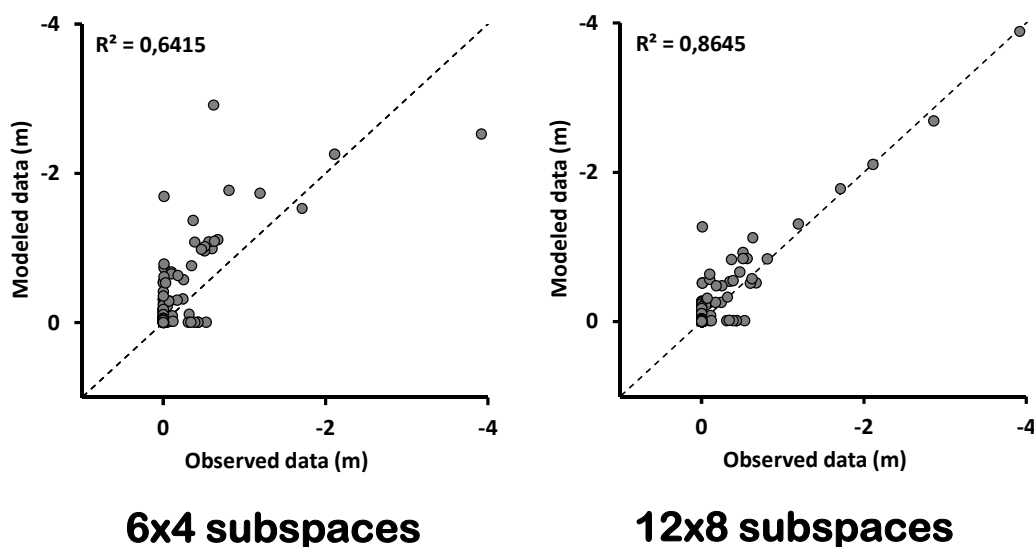
367 The fracture network in the model, however, cannot reproduce the known high connectivity
368 existing between some boreholes of the field (see Figure 1c). Two remarks can be proposed to
369 explain this limitation. First, the DNDI method limits the directions of fractures to four possible
370 orientations, which constrains the liberty for the fracture network optimization. One possibility
371 to reduce this limitation is a more important partitioning of the model (for example in our case
372 by continuing our inversion process with a 24×16 partitioning). However, the more the model
373 is partitioned, the more the inversion computation time will be important, as this will necessarily
374 increase the amount of subspaces in the model and thus the amount of parameters to be inverted.
375 Secondary, as suggested in Fischer et al. (2018b), steady-state responses are influenced by flows
376 in all fractures and karstic structures of the field. This might 'hide' the information about the
377 flows associated to the most important flowpath (usually associated to conduits) in the
378 responses.

379

380 **4.2. Discussion**

381 During the inversion presented in this article, we performed a progressive multi-scale
382 partitioning. We started the inversion with a 6×4 subspaces and used the result of this first
383 inversion as initial model for a second inversion with a model repartitioned to 12×8 subspaces.
384 Figure 6 compares the scatterplots of observed/modeled drawdowns obtained after each
385 inversion. It shows that having a second partitioning to 12×8 subspaces was necessary to reach
386 an acceptable reproduction of the observed drawdowns (R^2 of 0,86). This is mainly due to the
387 gain of liberty in the optimization obtained from a finer partitioning of the model. However,
388 starting from a coarser partitioning with 6×4 subspaces, instead of directly inverting a 12×8
389 subspaces model, also presents the advantage of finding more quickly the main directions in
390 the fracture network. This is especially interesting as we chose to initiate the inversion with a

391 very simple model. It would have necessitate much more iterations to optimize the fracture
 392 network if we would have directly started with a finer partitioning.



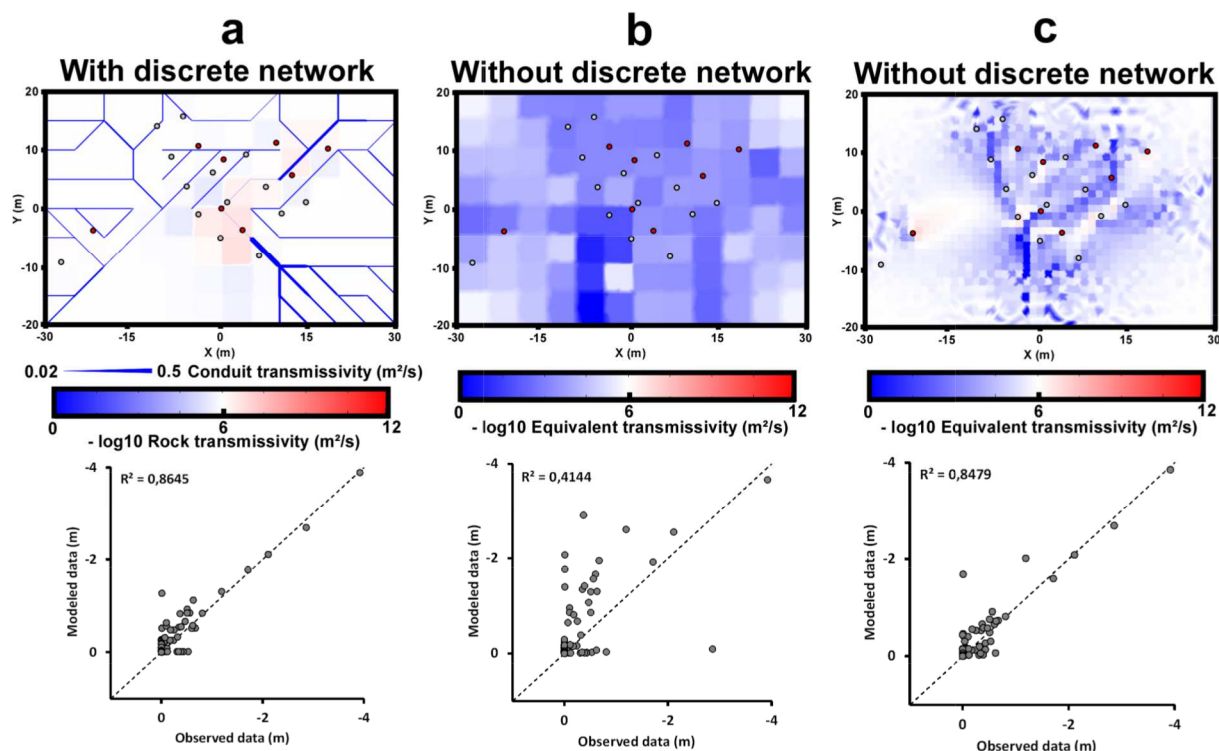
393

394 Figure 6: Scatterplots comparing the observed drawdowns to the drawdowns modeled with the
 395 distributed models obtained as results of the inversions for a 6×4 partitioning and 12×8
 396 partitioning (presented in Figure 3).

397

398 In order to discuss the advantages brought by coupled model for the modeling of fractures
 399 fields, we compare the result obtained with the DNDI method, with a discrete network
 400 integrated in the model, to results obtained with equivalent porous media models. Therefore we
 401 have also performed inversions with model without a discrete network. In these cases the
 402 inversions were performed in a same way then the DNDI method but without the discrete
 403 network part in the model (\mathbf{P}_{Dir}) and without the structural inversion part of Eq.3 (thus, were
 404 limited to the minimization of the hydraulic properties of the continuum in Eq.4 through its
 405 linearization in Eq.7). Figure 7 presents the inversion results (transmissivity maps and
 406 scatterplots) obtained from the DNDI method, and two results obtained from inversions of
 407 models without discrete network: one at the same partitioning (12×8) than the DNDI result
 408 and one reaching an equivalent ability of reproduction of the observed data but with a finer

409 partitioning (48×32). It can be noted that the computation times necessary to obtain these
410 different results are proportional to their complexity (several days for the DNDI solution in
411 Figure 7a, about one day for the solution of Figure 7c and a few hours for the one of Figure 7b).
412 By comparing the result obtained with the DNDI method (Figure 7a) to the equivalent porous
413 medium result with a same partitioning (Figure 7b), it appears that the integration of a discrete
414 network at this partitioning is crucial. In fact, without integrating fractures in the model, the
415 inversion fails at finding a distribution able to reproduce the observed drawdowns, even though
416 transmissivity values are set at high values in the model in order to simulate the
417 fractures/conduits flows. These flows are locally constrained and, thus, a fine distribution of
418 the properties is needed in the model in order to permit their simulation. A model without a
419 discrete network but with a finer resolution (Figure 7c) is able to reproduce these flows and
420 their induced drawdowns, but it would require a much finer partitioning (48×32) than the
421 DNDI model (12×8). Furthermore, if some structures and fracture connectivity patterns may
422 be identifiable in such model, the distribution of the transmissivities remains rather smooth
423 (contrarily of the awaited contrasted distribution in fractured fields) and the values of
424 transmissivities globally high, unlike in the DNDI result which allows for a good contrast
425 between the fractures and the matrix. The coupled discrete-continuum model proposed with the
426 DNDI method appears, thus, as really interesting to image the properties of a fractured medium,
427 as it allows for a simulation of the complex flows even with a coarse partitioning of the model
428 and it generated a contrasted distribution of transmissivities which also permits to characterize
429 heterogeneity in the background matrix.



430

431 Figure 7: Maps of transmissivity distributions and associated reproduction of observed
 432 drawdowns (scatterplots) obtained after inversions with a model taking into account a discrete
 433 network (a), or with equivalent porous media models at two different property grids resolution
 434 (12×8 (b) and 48×32 subspaces (c)).

435

436 An alternative to represent the contrast of hydraulic properties from a fractures/karstic field
 437 without integrating a discrete network in the model has been proposed in Fischer et al. (2017b)
 438 by applying a Cellular Automata-based Deterministic Inversion (CADI) method. This
 439 application was led on the same site and with the same dataset than the one presented in this
 440 article, which permits an interesting comparison between the two methods. The CADI method,
 441 unlike the DNDI, is based on a single continuum approach in which the fracture network is
 442 structured directly within the property field with cellular automata. It allows for more liberty in
 443 the structural optimization of the property distribution than the DNDI method. Therefore the
 444 network represented in the CADI result is more realistic regarding the knowledge of the field.
 445 It permits, for example, the reproduction of the known high connectivity between some
 446 boreholes, represented in Figure 1c. However, and as discussed before with Figure 7, the result

447 obtained with the DNDI method permits a better reproduction of the flows and the observed
448 drawdowns, even with a coarser partitioning ($R^2=0,86$ with 12×8 subspaces for the DNDI
449 model and $R^2=0,78$ with 24×16 subspaces for the CADI model in Fischer et al. (2017b)).

450

451 **5. Conclusion**

452 We present an application of a hydraulic tomography led on the fractured and karstic Terrieu
453 field site in France in order to image its transmissivity field in a model. The dataset consists in
454 drawdown responses to pumping tests reaching the pseudo steady state. The inversion was
455 performed with the DNDI method, a method that allows for the optimization of the distribution
456 of transmissivities in the model, but also for the optimization of the structure of a discrete
457 network in the model.

458 The model obtained after inversion of the dataset permits a good reproduction of the observed
459 drawdowns and also reproduces the main directions of fracturing observed on the field, even
460 though this information was not included in the inversion process. However, the model fails at
461 reproducing the known high connectivity (conduit flows) in the field. This may be due to the
462 limitations of the DNDI method concerning the possible orientations of fractures for the
463 optimization, but also to the flow information contained in the steady state drawdown responses
464 which might not permit to distinguish the major flowpaths from less important ones.

465 The results obtained with the DNDI method on this application show two main advantages of
466 using a coupled discrete-continuum model for the characterization of the flows in fractured
467 media, compared to equivalent porous media models. The discrete network in the model allows
468 for a better contrast in the transmissivity distribution and induces a better reproduction of the
469 observed drawdowns, with a coarser partitioning of the model that would be needed with an
470 equivalent porous medium model. The contrast existing in a coupled model also allows for

471 more details in the background of the model (matrix), whereas in equivalent porous media
472 models the distinction between structures (fracture/conduit) and matrix is less clear.

473 The DNDI method can be applied to other types of hydraulic data simply by adapting the
474 forward problem and the data used in the inversion. For example it could be possible to lead a
475 same type of modeling with drawdown curves in a time domain, or with oscillatory response in
476 a frequency domain (as proposed in Fischer et al. 2018b). Nevertheless, the DNDI method still
477 requires some improvement in order to provide more liberty in the structural optimization of
478 the network. With more liberty, the results could provide even better localization and
479 positioning of the fractures, without having to increase the partitioning of the model (which
480 leads to more computation time). Furthermore, at the moment this method has developed only
481 in 2D, and would require some additions to work in 3D.

482

483 **Acknowledgments**

484 We thank Lisa Ringel, Peter Bayer and Maria Klepikova for their relevant comments and
485 suggestions to improve the quality of this article. Data and characterization of the Terrieu
486 experimental site was realized within the framework of the MEDYCYSS observation site, part
487 of the Karst observatory network initiated by the French institute INSU/CNRS. Data are
488 available on demand on www.sokarst.org.

489 **References**

490 Batu, V. 1998. *Aquifer Hydraulics: A Comprehensive Guide to Hydrogeologic Data Analysis*.
491 John Wiley and Sons, New York.

492

493 Butler, J.J. 2005. Hydrogeological methods for estimation of spatial variations in hydraulic
494 conductivity. In: Rubin, Y., S.S. Hubbard. *Hydrogeophysics*. Water Science and Technology
495 Library (vol. 50). Springer, Dordrecht.

496

497 Bonneau, F., V. Henrion, G. Caumon, P. Renard, J. Sausse. 2013. A Methodology for Pseudo-
498 Genetic Stochastic Modeling of Discrete Fracture Networks. *Computers and Geosciences* 56:
499 12-22.

500

501 Cacas, M.C., E. Ledoux, G. de Marsily, B. Tillie, A. Barbreau, E. Durand, B. Feuga, P.
502 Peaudecerf. 1990. Modeling Fracture Flow With a Stochastic Discrete Fracture Network:
503 Calibration and Validation. 1. The Flow Model. *Water Resources Research* 26: 479-489.

504

505 Cardiff, M., W. Barrash. 2011. 3-D transient hydraulic tomography in unconfined aquifers with
506 fast drainage response. *Water Resources Research* 47: W12518.

507

508 Cardiff, M., W. Barrash, P.K. Kitanidis. 2013. Hydraulic conductivity imaging from 3-D
509 transient hydraulic tomography at several pumping/observation densities. *Water Resources*
510 *Research* 49: 7311-7326.

511

512 Dausse, A. 2015. Facteurs d'échelle dans la hiérarchisation des écoulements au sein d'un
513 aquifère karstique: Analyse multi-échelles des propriétés hydrodynamiques et de transport de
514 l'aquifère de Lez. PhD thesis, French. Université de Montpellier.

515

516 Dausse, A., V. Leonardi, H. Jourde. 2019. Hydraulic characterization and identification of flow-
517 bearing structures based on multi-scale investigations applied to the Lez karst aquifer. *Journal*
518 *of Hydrology Regional Studies* Accepted.

519

520 Dong, Y., T. Fu, T.-C.J. Yeh, Y.-L. Wang, Y. Zha, L. Wang, Y. Hao. 2019. Equivalence of
521 discrete fracture network and porous media models by hydraulic tomography. *Water Resources*
522 *Research* 55: 3234-3247.

523

524 Fischer, P., A. Jardani, A. Soueid Ahmed, M. Abbas, X. Wang, H. Jourde, N. Lecoq. 2017a.
525 Application of large-scale inversion algorithms to hydraulic tomography in an alluvial aquifer.
526 *Groundwater* 55: 208-218.

527

528 Fischer, P., A. Jardani, X. Wang, H. Jourde, N. Lecoq. 2017b. Identifying flow networks in a
529 karstified aquifer by application of the cellular automata-based deterministic inversion method
530 (Lez aquifer, France). *Water Resources Research* 53: 10508-10522.

531

532 Fischer, P., A. Jardani, N. Lecoq. 2018a. Hydraulic tomography of discrete networks of
533 conduits and fractures in a karstic aquifer by using a deterministic inversion algorithm.
534 *Advances in Water Resources* 112: 83-94.

535

536 Fischer, P., A. Jardani, H. Jourde, M. Cardiff, X. Wang, S. Chedeville, N. Lecoq. 2018b.
537 Harmonic pumping tomography applied to image the properties and interpret the connectivity
538 of a karstic and fractured aquifer (Lez aquifer, France). *Advances in Water Resources* 119: 227-
539 244.

540

541 Grimstad, A.-A., T. Mannseth, G. Naevdal, H. Urkedal. 2003. Adaptive multiscale
542 permeability estimation. *Computers & Geosciences* 7 (No. 1):1-25.

543

544 Hao, Y., T.-C.J. Yeh, J. Xiang, W.A. Illman, K. Ando, K.-C. Hsu, C.-H. Lee. 2008. Hydraulic
545 Tomography for Detecting Fracture Zone Connectivity. *Ground Water* 46: 183-192.

546

547 Illman, W.A., X. Liu, S. Takeuchi, T.-C.J. Yeh, K. Ando, H. Saegusa. 2009. Hydraulic
548 tomography in fractured granite: Mizunami Underground Research site, Japan. *Water*
549 *Resources Research* 45: W01406.

550

551 Illman, W.A. 2014. Hydraulic Tomography Offers Improved Imaging of Heterogeneity in
552 Fractured Rocks. *Groundwater* 52: 659-684.

553

554 Jazayeri Noushabadi, M.R. 2009. Characterization of relationship between fracture network
555 and flow-path network in fractured and karstic reservoirs: Numerical modeling and field
556 investigation (Lez aquifer, Southern France). PhD thesis, English. Université de Montpellier.

557

558 Jazayeri Noushabadi M.R., H. Jourde, G. Massonnat. 2011. Influence of the observation scale
559 on permeability estimation at local and regional scales through well tests in a fractured and
560 karstic aquifer (Lez aquifer, Southern France). *Journal of Hydrology* 403: 321-336.

561

562 Josnin, J.Y., H. Jourde, P. Fenart, P. Bidaux. 2002. A three-dimensional model to simulate joint
563 networks in layered rocks. *Canadian journal of Earth Sciences* 39: 1443-1455.

564

565 Jourde, H., C. Batiot-Guilhe, V. Bailly-Comte, C. Bicalho, M. Blanc, V. Borrell, C. Bouvier,
566 J.F. Boyer, P. Brunet, M. Cousteau, C. Dieulin, E. Gayrard, V. Guinot, F. Hernandez, L. Kong
567 A Siou, A. Johannet, V. Leonardi, N. Mazzilli, P. Marchand, N. Patris, S. Pistre, J.L. Seidel,
568 J.D. Taupin, S. Van-Exter. 2011. The MEDYCYSS observatory, a multi scale observatory of
569 flood dynamics and hydrodynamics in karst (Mediterranean border Southern France). In:
570 Lambrakis, N., G. Stournaras, K. Katsanou. Advances in the research of aquatic environment.
571 *Environmental Earth Sciences*. Springer, Berlin, Heidelberg.

572

573 Jourde, H., N. Massei, N. Mazzilli, S. Binet, C. Batiot-Guilhe, D. Labat, M. Steinmann, V.
574 Bailly-Comte, J.L. Seidel, B. Arfib, J.B. Charlier, V. Guinot, A. Jardani, M. Fournier, M.
575 Aliouache, M. Babic, C. Bertrand, P. Brunet, J.F. Boyer, J.P. Bricquet, T. Camboulive, S.D.
576 Carrière, H. Celle-Jeanton, K. Chalikakis, N. Chen, C. Cholet, V. Clauzon, L. Dal Soglio, C.

577 Danquigny, C. Défargue, S. Denimal, C. Emblanch, F. Hernandez, M. Gillon, A. Gutierrez, L.
578 Hidalgo Sanchez, M. Hery, N. Houillon, A. Johannet, J. Jouves, N. Jozja, B. Ladouche, V.
579 Leonardi, G. Lorette, C. Loup, P. Marchand, V. de Montety, R. Muller, C. Ollivier, V. Sivelles,
580 R. Lastennet, N. Lecoq, J. C. Maréchal, L. Perotin, J. Perrin, M.A. Petre, N. Peyraube, S. Pistre,
581 V. Plagnes, A. Probst, J.L. Probst, R. Simler, V. Stefani, D. Valdes-Lao, S. Viseur, X. Wang.
582 2018. SNO KARST: A French Network of Observatories for the Multidisciplinary Study of
583 Critical Zone Processes in Karst Watersheds and Aquifers. *Vadose Zone Journal* 17: 180094.

584

585 Klepikova, M., T. Le Borgne, O. Bour, J.-R. de Dreuzy. 2013. Inverse modeling of flow
586 tomography experiments in fractured media. *Water Resources Research* 49: 7255-7265.

587

588 Klepikova, M., T. Le Borgne, O. Bour, K. Gallagher, R. Hochreutener, N. Lavenant. 2014.
589 Passive temperature tomography experiments to characterize transmissivity and connectivity of
590 preferential flow paths in fractured media. *Journal of Hydrology* 512: 549-562.

591

592 Kovacs, A. 2003. Estimation of conduit network geometry of a karst aquifer by the means of
593 groundwater flow modeling (Bure, Switzerland). *Boletín Geológico y Minero* 114: 183-192.

594

595 Mohammadi, Z., W.A. Illman. 2019. Detection of karst conduit patterns via hydraulic
596 tomography: A synthetic inverse modeling study. *Journal of Hydrology* 572: 131-147.

597

598 Pardo-Iguzquiza, E., P.A. Dowd, C. Xu, J.J. Duran-Valsero. 2012. Stochastic simulation of
599 karst conduit networks. *Advances in Water Resources* 35: 141-150.

600

601 Sharmeen, R., W.A. Illman, S.J. Berg, T.-C.J. Yeh, Y.-J. Park, E.A. Sudicky, K. Ando. 2012.
602 Transient hydraulic tomography in a fractured dolostone : Laboratory rock block experiments.
603 *Water Resources Research* 48: W10532

604

605 Somogyvari, M., M. Jalali, S. Jimenez Parras, P. Bayer. 2017. Synthetic fracture network
606 characterization with transdimensional inversion. *Water Resources Research* 53: 5104-5123.

607

608 Tarantola, A. and B. Valette. 1982. Generalized nonlinear inverse problems solved using the
609 least squares criterion. *Reviews of Geophysics and Space Physics* 20 (No. 2): 219-232.

610

611 Tiedeman, C.R., W. Barrash. 2019. Hydraulic tomography: 3D hydraulic conductivity, fracture
612 network, and connectivity in mudstone. *Groundwater* doi: 10.1111/gwat.12915.

613

614 Trottier, N., F. Delay, O. Bildstein, P. Ackerer. 2014. Inversion of a dual-continuum approach
615 to flow in a karstified limestone: Insight into aquifer heterogeneity revealed by well-test
616 interferences. *Journal of Hydrology* 508: 157-169.

617

- 618 Wang, X., A. Jardani, H. Jourde, L. Lonergan, J. Cosgrove, O. Gosselin, G. Massonnat. 2016.
619 Characterisation of the transmissivity field of a fractured and karstic aquifer, Southern France.
620 *Advances in Water Resources* 87: 106-121.
- 621
- 622 Wang, X., A. Jardani, H. Jourde. 2017. A hybrid inverse method for hydraulic tomography in
623 fractured and karstic media. *Journal of Hydrology* 551: 29-46.
- 624
- 625 Yeh, T.-C.J., S. Liu. 2000. Hydraulic tomography: Development of a new aquifer test method.
626 *Water Resources Research* 36: 2095-2105
- 627
- 628 Yeh, T.-C.J., C.-H. Lee. 2007. Time to change the way we collect and analyze data for aquifer
629 characterization. *Ground Water* 45: 116-118.
- 630
- 631 Yoon, S., A.H. Malallah, A. Datta-Gupta, D.W. Vasco, R.A. Behrens. 1999. A multiscale
632 approach to production data integration using streamline models. *Society of Petroleum*
633 *Engineers* 56653, in: 1999 SPE Annual Technical Conference and Exhibition, SPE 56653.
- 634
- 635 Zha, Y., T.-C.J. Yeh, W.A. Illman, T. Tanaka, P. Bruines, H. Onoe, H. Saegusa. 2015. What
636 does hydraulic tomography tell us about fractured geological media? A field study and synthetic
637 experiments. *Journal of Hydrology* 531: 17-30.